THE JOURNAL OF PHYSICAL CHEMISTRY C
A JOURNAL OF THE AMERICAN CHEMICAL SOCIETY

pubs.acs.org/JPCC

Article

# Insights into the Molecular Structure of $MoO_x$ Catalysts via Static and Transient Raman Experimentation

Thu D. Nguyen, Alfred Worrad, Dhanush Thirulogachandar, Fuat E. Celik, Stavros Caratzoulas, and George Tsilomelekis*

Cite This: *J. Phys. Chem. C* 2024, 128, 9169−9181

Read Online

ACCESS | Metrics & More | Article Recommendations | Supporting Information

**ABSTRACT:** A comprehensive framework is developed for the study of the molecular configuration of $(MoO_x)_n$ species supported on pure anatase-$TiO_2$ as well as on mixed $CeO_2$−$TiO_2$. The framework first employs the equilibrium deposition filtration method to molecularly control the nature of the active molybdenum sites on the surface of the supports while ensuring loadings below monolayer coverage. Next, we deploy in situ Raman spectroscopic characterization in combination with the isotope $^{18}O_2/^{16}O_2$ exchange technique for the molecular-level identification of $(MoO_x)_n$ surface configurations. Results show that the distribution of $(MoO_x)_n$ species depends strongly on the pH of the precursor solution and that on both the $TiO_2$ and $CeO_2$−$TiO_2$ supports, the dominant configuration pertains to a mono-oxo arrangement. Distinctive spectral behaviors of a multicomponent band in the vicinity of the ∼900 $cm^{-1}$ band for supported $(MoO_x)_n$ on $CeO_2$−$TiO_2$ are assigned to two separate vibrational modes that involve different anchoring Mo-O-*Support* bonds. The framework also extends to the coupling of pulse experimentation with operando Raman spectroscopy (transient operando spectroscopy) to distinguish the reactivity among oxygen sites. From the rationalization of combined results, we show that upon $H_2$ exposure, the initial removal of surface oxygen predominantly happens at the terminal (Mo═O) site, which is then followed by the breaking of some Mo-O-*Support* bonds. This mechanism allows for oxygen swapping between different Mo−O bonds during reoxidation.

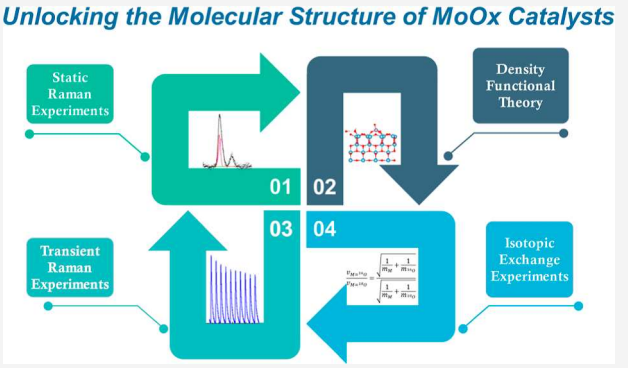




## INTRODUCTION

In recent decades, there has been growing interest in the use of supported molybdenum catalysts owing to their outstanding performance in various processes.[1−24] Multiple attempts have been made to enhance the reactivity of active molybdenum sites[13,18,25−28] through modification of their physicochemical properties either by using promoters or a mixed-oxide support phase. However, the simultaneous presence of multiple species with potentially different reactivities may lead to ambiguous interpretations about the link between the synthesis and performance of oxide catalysts. Investigations of the group of transition metal oxides supported on $SiO_2$ have indicated the prevalence of isolated metal oxide species in the dioxo configuration on silica,[29−35] particularly at low coverages. On the other hand, more complex structures are present on $Al_2O_3$, $ZrO_2$, and $TiO_2$, where the dispersion is much higher; the simultaneous formation of both isolated and polymeric domains is also well reported.[2,7,8,35−39]

Among the strategies to understand the issue of heterogeneity in dispersed oxide sites, in situ vibrational spectroscopy[7,40−49] has proved to be a powerful tool, able to provide molecular-level information on the structural response of deposited oxometallic phases. Particularly, both Raman and infrared (IR) spectroscopies have revealed that the arrangement of dispersed oxomolybdenum species can vary greatly, especially when deposited on different metal oxide supports. $^{18}O$ isotopic labeling has also been applied in conjunction with in situ Raman and IR studies to distinguish between mono-oxo, dioxo, or trioxo configurations on various surfaces.[48,50−55] The results from the isotopic exchange experimental framework, along with density functional theory (DFT) calculations, have shown that the dioxo species are favored on $MoO_3/SiO_2$,[31,56−58] the mono-oxo tetragonal pyramidal configuration is dominant on $\gamma$-alumina,[59−61] while the mono-oxo tetrahedral arrangement is the most stable configuration on $TiO_2$.[62−64]

Despite extensive endeavors in the literature and the unquestionable progress in the field, disentangling the distinct features of the plausible $(MoO_x)_n$ structures is still elusive, impeding our efforts to connect the three important pillars of

Received: March 28, 2024
Revised: May 14, 2024
Accepted: May 15, 2024
Published: May 23, 2024

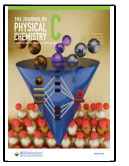




https://doi.org/10.1021/acs.jpcc.4c02018
J. Phys. Chem. C 2024, 128, 9169−9181

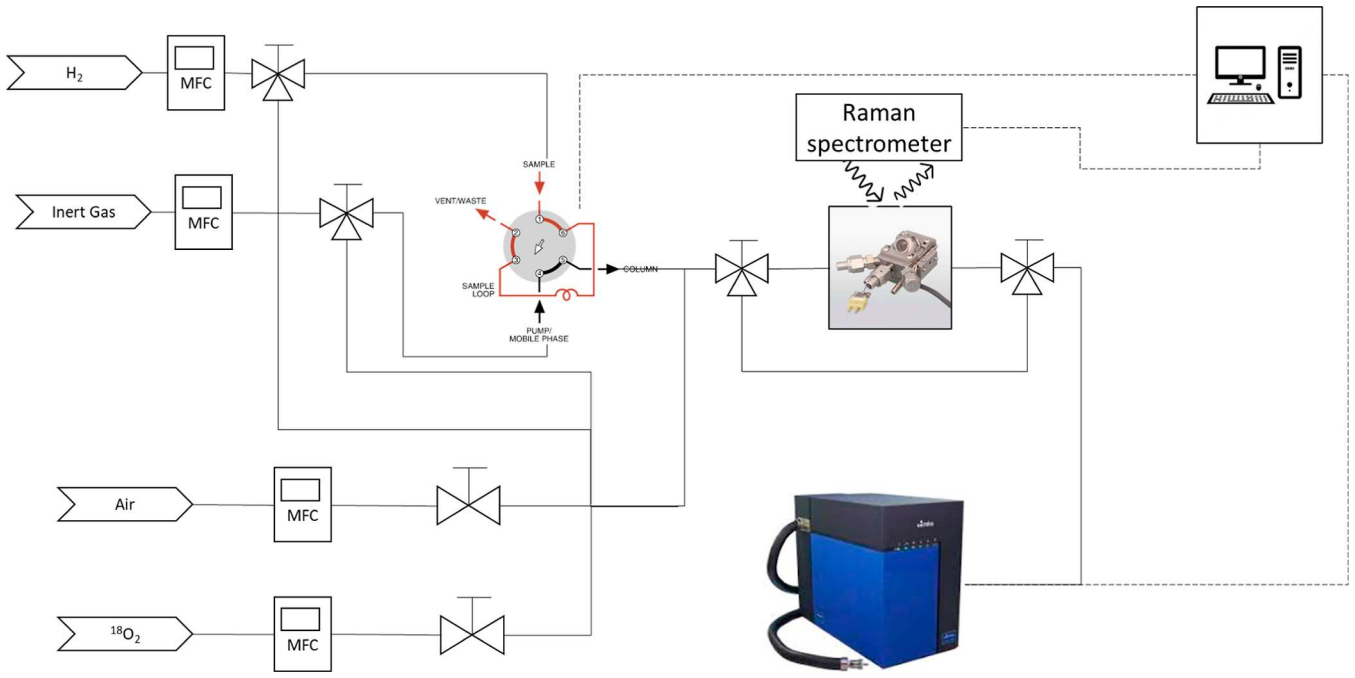


**Figure 1.** Schematic process flow diagram of the experimental apparatus for steady-state or transient in situ/operando Raman spectroscopic measurements.

catalysis, i.e., synthesis, surface species, and reactivity, toward the establishment of predictive structure−function relationships. Studies have primarily been restricted to well-defined, commercially available pure support oxides, leaving more complex but rather physicochemically interesting classes of catalysts such as supported mixed oxides or doped materials unexplored. Moreover, even within the same oxide configuration, the heterogeneity as well as the nearest-neighbor environment of M-O sites is chemically different, which in turn is expected to influence the reactivity.

To this extent, this study aims to provide a methodological experimental and computational framework, starting with a well-controlled synthesis method for the preparation of amorphous surface species. In this work, $(MoO_x)_n$ sites have been deposited on mixed $CeO_2$−$TiO_2$ and commercial anatase $TiO_2$ by using the equilibrium deposition filtration (EDF) method. The prevalence of distinct surface structures is studied by means of in situ Raman spectroscopy coupled with selective isotopic labeling to provide a connection between the material preparation and surface configurations. Relevant spectroscopic results are complemented by DFT calculations on model systems to assist with the species identification. Building on our previous efforts to investigate the $MoO_x/CeO_2$−$TiO_2$ catalysts for redox reactions,[26] the order and mechanism of oxygen site removal and substitution are also discussed.

## EXPERIMENTAL SECTION

**Catalyst Preparation and Characterization.** Metal precursors including $Ce(NO_3)_3{\cdot}6H_2O$ (99.99%), $Ti(OCH_2CH_2CH_2CH_3)_4$ (97%), $(NH_4)_6Mo_7O_{24}{\cdot}4H_2O$ (99.98%), and reference support pure anatase $TiO_2$ (catalog number: 044429.30) were obtained from Thermo Fisher. The detailed synthesis procedure for the mixed $CeO_2$−$TiO_2$ support via a sol−gel route can be found elsewhere.[65,66] Typically, in sol−gel synthesis, solution A was prepared by vigorously stirring a mixture of 10 g of $Ti(OC_4H_9)_4$, 3 mL of $CH_3COOH$, and 40 mL of $C_2H_5OH$. The pH of the solution was then adjusted to 2−3 via the dropwise addition of $HNO_3$. For solution B, the amount of $Ce(NO_3)_3$ was dissolved in 4 mL of deionized $H_2O$ and 20 mL of $C_2H_5OH$. Solution B was then added dropwise to solution A under vigorous stirring to form a transparent, homogeneous solution. The resulting solution was aged at room temperature for 1 h and then heated up to 70 °C, where it was kept for 2 h in order to form a gel. The concentration of solution B was varied accordingly to modify the Ce content of the resultant material. The gel was dried at 70 °C for 72 h, and the remaining solid underwent calcination at 600 °C in the presence of 100 mL/min air for 4 h with a ramp rate of 2 °C/min. The synthesized $CeO_2$−$TiO_2$ mixtures were labeled as $x$CeTi, where $x$ was formulated as

$$x = \frac{n_{Ce}}{n_{Ti}} \times 100\%$$

Molybdenum oxide was deposited on pure anatase $TiO_2$ and mixed $CeO_2$−$TiO_2$ supports by the EDF method. Detailed steps and rationale behind the synthesis procedure could be found in previous reports by Lycourghiotis et al.[67−77] Generally, the support oxide is added to 100 mL of an aqueous solution of $(NH_4)_6Mo_7O_{24}{\cdot}4H_2O$ under strong stirring. The pH of the suspension is adjusted with ammonia solution or nitric acid. After stabilization, the suspension is vacuum filtered and then dried overnight. The dried powder is then calcined at 600 °C in air for 4 h to remove organic compounds. The obtained supported Mo on $TiO_2$ and on $CeO_2$−$TiO_2$ are labeled as MoTi$y$ and MoCeTi$y$, respectively, where $y$ represents the pH during the EDF process.

**BET Measurements.** The specific surface area of the prepared oxide support was estimated through the Brunauer−Emmett−Teller (BET) method using a Quantachrome Autosorb-1 instrument. The BET measurements were carried out under cryogenic conditions after degassing the samples at


https://doi.org/10.1021/acs.jpcc.4c02018
J. Phys. Chem. C 2024, 128, 9169−9181

150 °C for 3 h for the complete removal of chemisorbed water on the surface.

**In Situ Raman Spectroscopy and $^{18}O/^{16}O$ Exchange.** The Raman spectroscopic investigations were conducted by utilizing a high spatial and spectral resolution HORIBA LabRAM HR Evolution spectrometer. The samples were irradiated with an incident beam at a wavelength of 532 nm and a power of 80 mW, which was directed and focused by a long-working-distance objective with a magnification of 50×. To maintain a low laser power at the sample location, neutral density filters were utilized, ensuring that the laser power did not exceed 8 mW on the sample. Collection of the scattered light was accomplished with an air-cooled open electrode charge-coupled device, having a resolution of 1024 × 256 pixels and operating at a temperature of −75 °C. The acquisition time and total number of accumulations were modulated within the ranges of 20−30 and 10−30 s, respectively. In situ Raman measurements were conducted by directing the laser line into a reaction cell manufactured by Harrick Scientific Products Inc. The total gas flow was controlled through a mass flow controller from Alicat Scientific. To minimize temperature gradients and ensure thermal stability, only a thin layer of the sample was loaded into the sample holder of the Harrick cell. The isotopic $^{18}O$ substitution process includes the flow of diluted 2% $H_2$ in Ar followed by the flushing phase of Ar flow at 50 mL/min and then a flow of 2% $^{18}O_2$ in Ar. All in situ spectra were collected at 600 °C.

**Transient Operando Raman Spectroscopy Measurements.** Operando Raman experiments were carried out by coupling the acquisition of a Raman spectrometer and an online mass spectrometer (Cirrus 3-XD Atmospheric Gas Analyzer, Quadrupole MS). The gas system is connected to a pulse system including a 2-position, 6-port valve with a 1.2 mL sampling loop (Vici Valco) modulated by an electric motor. The switching and resting times of the valve in its two positions are controlled by an Uno Arduino electronic board. At position A of the valve, the optical reactor is flushed with pure Ar flow, while at position B, this flow of Ar pushes 1.2 mL of diluted $H_2$ into the optical reactor to then be detected by the MS. The schematics of the experimental apparatus for the in situ and operando Raman spectroscopic measurements are illustrated in Figure 1.

The parameter set of the operando experiment was tuned to align both analytical and spectroscopic detections within a reasonable flow regime. While a peak-like signal caused by pulsing $H_2$ through the bypass was almost symmetric because of the plug flow nature, the pulse signal of $H_2$ and the consequentially formed $H_2O$ can significantly deviate from the ideal shape due to dead volume from the optical reactor (increased residence time, $\tau$). To mitigate the deviation from the ideal plug flow, the flow rate of sweep gas is required to be sufficiently high. However, the upper bound of the sweep gas flow rate is limited by the sensitivity of the analytical detector and the amount of material loaded into the optical reactor. Likewise, the Raman spectrum acquisition time was always much slower than the MS scanning time. To synchronize the spectroscopic and analytical acquisition, the blank time between each pulse was extended to at least two times the total acquisition time of a Raman spectrum. Typically, 0.01 g of the material was loaded into the optical reactor. The flow rate of sweep gas was set to 50 mL/min, while the $H_2$ concentration in the sampling loop was adjusted to 2%. The MS was set to scan only masses ($m/z$ = 2, 18, and 40) to maximize the data collection frequency. The Raman acquisition time and total number of accumulations were 60 and 10, respectively. Each pulse, including its subsequent blank time, was modulated to take 20 min in total.

**Computational Methods.** All DFT calculations were performed with the Quickstep module in CP2K 9.1.[78] The PBE exchange−correlation functional was utilized with the molecularly optimized (MOLOPT-DZVP-SR-GTH) double-$\zeta$ basis set,[79] Goedecker−Teter−Hutter (GTH) pseudopotentials,[80] a plane-wave cutoff of 600 Ry, and Grimme's D3 dispersion correction.[81] The (001) facet of anatase was investigated using a 4 × 4 supercell with lattice vectors 15.109 × 15.109 × 19.046 Å (upon addition of 10 Å vacuum in the $z$-direction). We chose to model the (001) facet as it has been previously reported that, due to its enhanced ability to dissociate water, surface species such as $H^+$ and $OH^-$ are more likely to be present on the (001) than on the (101) facet.[82] Due to the greater impact of pH on this facet, it follows that the anchoring of Mo species on this facet is more susceptible to variations in pH. Vibrational frequencies were obtained in the harmonic approximation for converged structures that satisfied a self-consistent field energy difference of $1 \times 10^{-8}$ Ha. For simulating $^{18}O$ species, selected oxygen atoms were set to have an atomic mass of 17.999 au. DFT + $U$ corrections were applied to Ti atoms with a Hubbard $U$ value of 7.25 eV to match the band gap of anatase (3.2 eV). The monomeric structure of $MoO_5$ was constructed by relaxing a $Mo^{(VI)}O_3$ unit to the surface and performing geometric relaxation. The $MoO_4$ model was constructed by taking the relaxed $MoO_5$ structure and removing the oxygen of a single Mo−O−Ti bridge to the support, producing a $Mo^{(V)}O_4$ and a nearby $Ti^{(III)}$. Dimer and trimer structures were constructed by adding 2 or 3 $MoO_3$ units in a similar fashion to the monomer. For the cyclic trimer model, a cyclic $Mo_3O_9$ structure was first relaxed in the gas phase before being brought to the surface. Due to the additional Mo−O−Mo connection, an additional water molecule was dissociated on the surface near the cluster to stabilize the dangling Ti−O ligand.

## RESULTS AND DISCUSSION

**$(MoO_x)_n$ Supported on Commercial Anatase-$TiO_2$.** Figure 2a shows the normalized Raman spectra of the series of $(MoO_x)_n$ catalysts supported on pure anatase $TiO_2$ at 600 °C in flowing air. The catalysts were prepared at different pH values of the precursor solution, inducing distinct changes in their vibrational features. The intensity of the Mo═O stretching mode increases monotonically as the synthesis pH decreases. This intensity increase is associated with the increase of the overall surface density (Mo/nm$^2$), which agrees with the results from our X-ray fluorescence (XRF) analysis (see Table S1). An attempt to deconvolute the molybdenyl stretching mode peak, which is located in the vicinity of ∼990 cm$^{-1}$, is also presented in Figure 2b−d for the catalysts prepared at pH values of 9, 6, and 4.

In order to achieve efficient deconvolution of the Mo═O spectral envelop (monitored by the residuals), at least three different component peaks were required; their individual positions are in agreement with the spectral range of supported molybdena catalysts on $TiO_2$ as reported in the literature and imply the presence of different dispersed species.[47−49,74,83−85] It is worth noting here that the relative contribution of the deconvoluted bands changes between catalysts prepared at different pH values, with a clear increase in the contribution of the species associated with the 992 cm$^{-1}$ mode as pH is decreased. This behavior clearly demonstrates that by adjusting


https://doi.org/10.1021/acs.jpcc.4c02018
J. Phys. Chem. C 2024, 128, 9169−9181

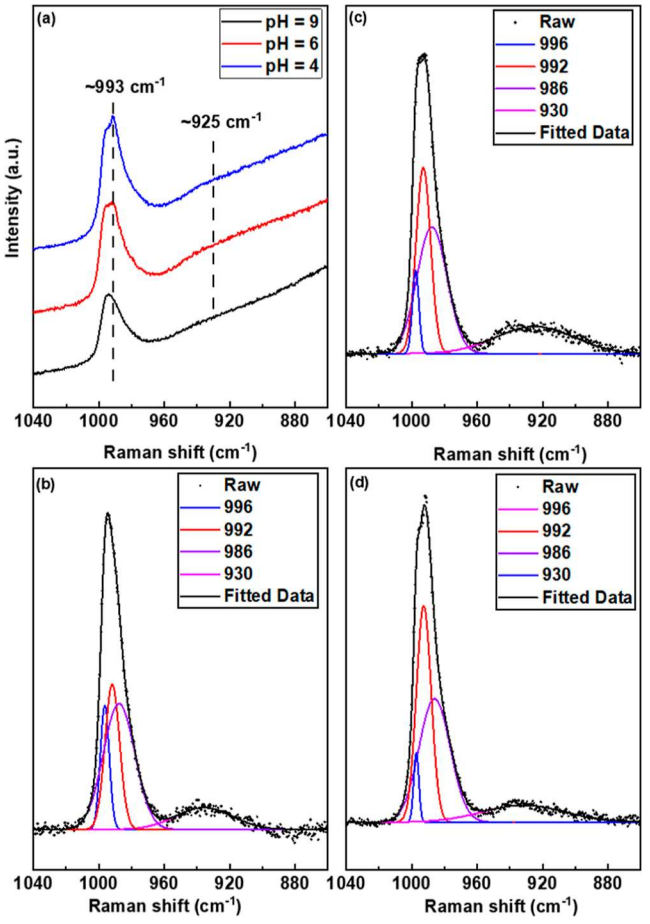


**Figure 2.** (a) Raman spectra of MoTi catalysts prepared by EDF in different pH solutions and calcined at 600 °C under air flow. Relevant peak deconvolution of the terminal oxygen band for (b) MoTi9, (c) MoTi6, and (d) MoTi4.

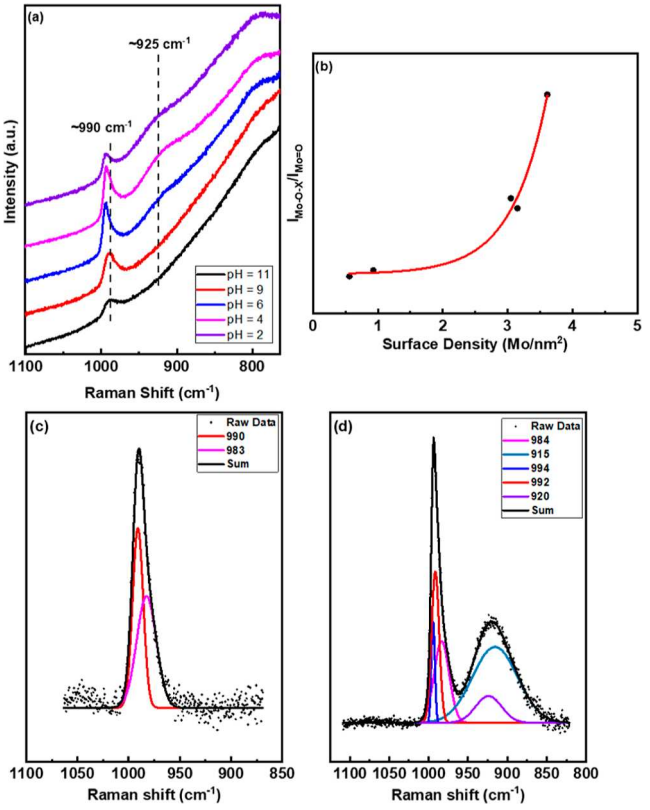


**Figure 3.** (a) Raman spectra of MoCeTi prepared by EDF at different pH solutions and calcined at 600 °C under air flow. (b) Peak intensity ratio of bridging/anchoring oxygen to molybdenyl oxygen versus surface density. (c,d) Peak deconvolution of the terminal oxygen band for MoCeTi9 and MoCeTi4.

the synthesis pH, the structure of the deposited phase can be controlled at the molecular level. Additionally, a careful look at the Raman spectra reveals the presence of a broad, but rather weak, band at around 900 $cm^{-1}$. This feature has been the focus of several literature reports due to its distinct behavior under the reaction conditions, and it is believed that it is associated with the stretching modes of Mo−O−X configurations, where X can be either another molybdenum atom (bridging bond in oligomers) and/or the cation of the support (anchoring bond).[7,23,32,41,48,49,52,53,55,63,73,74,83,86,87] Structural implications of this band are discussed in more detail in later sections.

**$(MoO_x)_n$ Supported on Synthesized $CeO_2$−$TiO_2$.** In the case of molybdena catalysts supported on $CeO_2$−$TiO_2$, as the synthesis pH decreases, the overall Mo loading increases, as shown by the XRF results in Table S1; this observation is similar to the trend seen in the family of supported catalysts on pure $TiO_2$. However, it is worth noting that the surface loadings for the supported molybdena catalysts on $CeTiO_2$ reach a plateau at ~3.9 Mo/$nm^2$, notably below the anticipated monolayer coverage, even though the pH of the precursor solution was significantly low.

Figure 3a displays the Raman spectra of $(MoO_x)_n$ supported on $CeTiO_2$, synthesized over a range of pH values. We observe that catalysts prepared at low pH exhibit a small shift to higher wavenumbers in the position of the terminal Mo═O band. Furthermore, as the pH decreases during synthesis, a band around ~900 $cm^{-1}$ (possible assignments discussed also previously) becomes more prominent. The intensity ratio of Mo−O−X to the intensity of the Mo═O feature ($I_{Mo-O-X}/I_{Mo=O}$) increases with increasing the surface density (see Figure 3c) or, in other words, increases as the synthesis pH decreases. The strong nonlinear correlation between the surface density and $I_{Mo-O-X}/I_{Mo=O}$ implies the weak coupling between coverage and the emergence of new surface species. Furthermore, the emergence of new species, signaled by $I_{Mo-O-X}/I_{Mo=O}$, coincides well with the pH range at which the Mo species in solution transforms into polymers. These observations imply a strong effect of pH through species induction in the solution during the synthesis on the final structures of $MoO_x$. In addition, a deconvolution of the Mo═O band, similar to what was undertaken in the previous section, was also performed on samples MoCeTi9 (Figure 3b) and MoCeTi4 (Figure 3d). A similar trend in the relative change of the deconvoluted Mo═O components is observed, where the high-frequency component increases in intensity in catalysts prepared at low pH. Interestingly, the 900 $cm^{-1}$ band requires two components for a deconvolution with good fidelity, thus highlighting the possibility of more than one feature present.

According to previous research, PZC of $TiO_2$ is around ~6,[88,89] while that of $CeO_2$ is commonly reported to be higher, that is, around 7−8.[90−92] It is expected that as the pH decreases, fewer OH groups on ceria will be deprotonated, hindering the formation of the Mo−O−Ce bond.[92−98] This comprises indirect evidence that one of the components of the ~900 $cm^{-1}$ band should not be associated with the anchoring oxygen


https://doi.org/10.1021/acs.jpcc.4c02018
J. Phys. Chem. C 2024, 128, 9169−9181

of molybdenum on ceria. On the other hand, at higher pH values, OH groups on ceria could also be deprotonated, thus making the formation of Mo−O−Ce more likely. However, considering that the total amount of Ce atoms in the support is 5% as compared to that in Ti, the Mo−O−Ce contribution to the spectral features should be significantly smaller than that of Mo−O−Ti. It is important to mention that although the amorphous ceria content in the bulk is expected to be very similar to that on the surface, precisely evaluating such surface compositional changes may require the utilization of more rigorous spectroscopic methods, such as IR-$CH_3OH$ chemisorption.[99] Furthermore, in our previous study,[26] we showed that on mixed $CeTiO_2$ oxide supports, $MoO_x$ is constrained to anchor mainly on titania facets, as observed by means of in situ DRIFTS through the respective titration of surface hydroxyl groups. Besides, background correction and deconvolution of the high pH samples (low loading) revealed no evidence of a spectral feature in the vicinity of 900 $cm^{-1}$. This consideration suggests the possible contribution of Mo−O−Mo features, alongside with the contribution of Mo−O−Ti, to the ∼900 $cm^{-1}$ band due to resonance coupling of confined $(MoO_x)_n$ species with different molecularities.[100]

**Isotopic Exchange Experiments and Surface Structure Confirmation of $(MoO_x)_n$ on $TiO_2$.** Figures 4a and 5a show the results of the isotopic $^{18}O$ substitution for MoTi9 and MoTi4, respectively, for two consecutive cycles of reduction

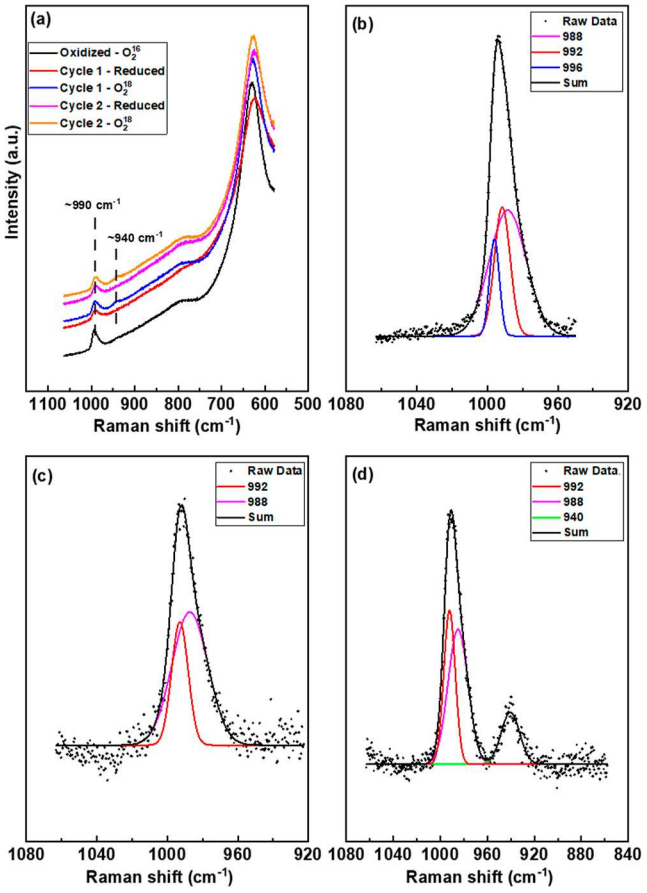


**Figure 4.** (a) Raman spectra of MoTi9 at different isotopic substitution cycles at 600 °C. (b−d) Deconvolution analysis of the terminal oxygen band for MoTi9 under air flow, under $H_2$ reduction conditions, and under $^{18}O_2$ flow, respectively.

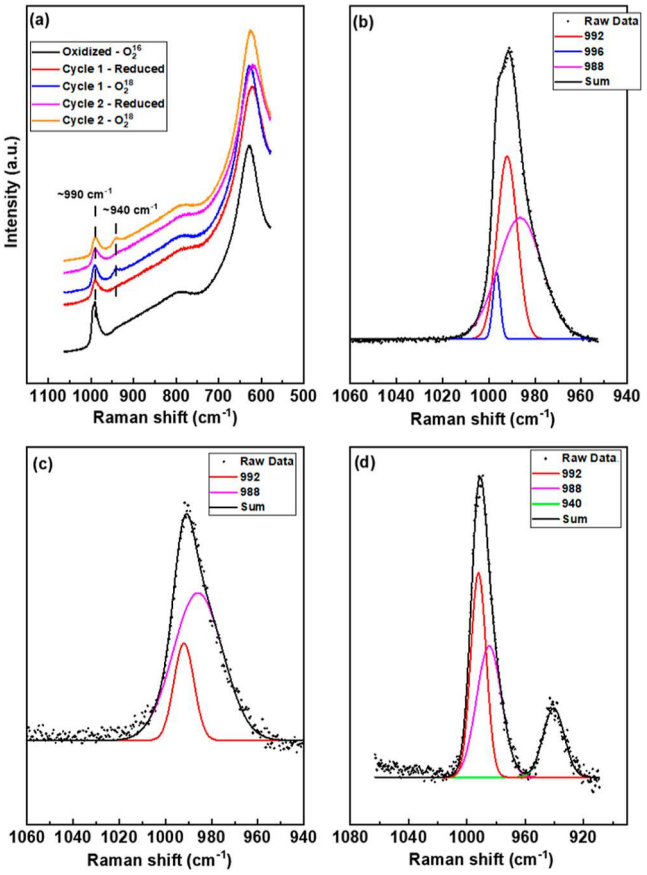


**Figure 5.** (a) Raman spectra of MoTi4 after different isotopic substitution cycles at 600 °C. (b−d) Deconvolution analysis of the terminal oxygen band for MoTi4 under air flow, under $H_2$ reduction conditions, and under $^{18}O_2$ flow, respectively.

with $H_2$ and reoxidation with $^{18}O$. Also, details of relevant spectral deconvolution for each isotopic substitution step, starting from fully oxidized condition with air flow, followed by reduction under $H_2$ and reoxidization with $^{18}O_2$ flow, are presented in Figures 4b−d and 5b−d for MoTi9 and MoTi4, respectively. Both materials exhibit the same spectral behaviors throughout the redox cycles. During the reduction phase, the Raman spectra of these materials were missing the 996 $cm^{-1}$ band, and this was accompanied by a decrease in the overall contribution of the 992 $cm^{-1}$ band as compared to that of the 988 $cm^{-1}$ band. This mere fact appears to be responsible for the apparent red shift in the enveloping molybdenyl band. This observation underscores the difference in the reducibility of the distinct Mo═O functionalities that originate from different species with distinguishing surroundings. Upon the isotopic substitution, a noticeable appearance of a new band around ∼940 $cm^{-1}$ was observed. Interestingly, upon deconvolution, only one Gaussian peak was required, highlighting that in the early stages of redox cycles, primarily, only one species was substituted. In addition, the mere appearance of the 940 $cm^{-1}$ band supports the assignment of the Mo surface configuration to be mono-oxo. This structural confirmation has also been reported for supported molybdenum on $TiO_2$, prepared by other synthesis methods such as incipient wetness impregnation or wet impregnation,[47−49,83,84] as well as supported $(MoO_x)_n$ on $Al_2O_3$ and $ZrO_2$.[2,7,49] Unexpectedly, during reoxidation with $^{18}O_2$, there was also a sign of recovery of some unsubstituted Mo═$^{16}O$ component peaks. However, the deconvolution


https://doi.org/10.1021/acs.jpcc.4c02018
J. Phys. Chem. C 2024, 128, 9169−9181

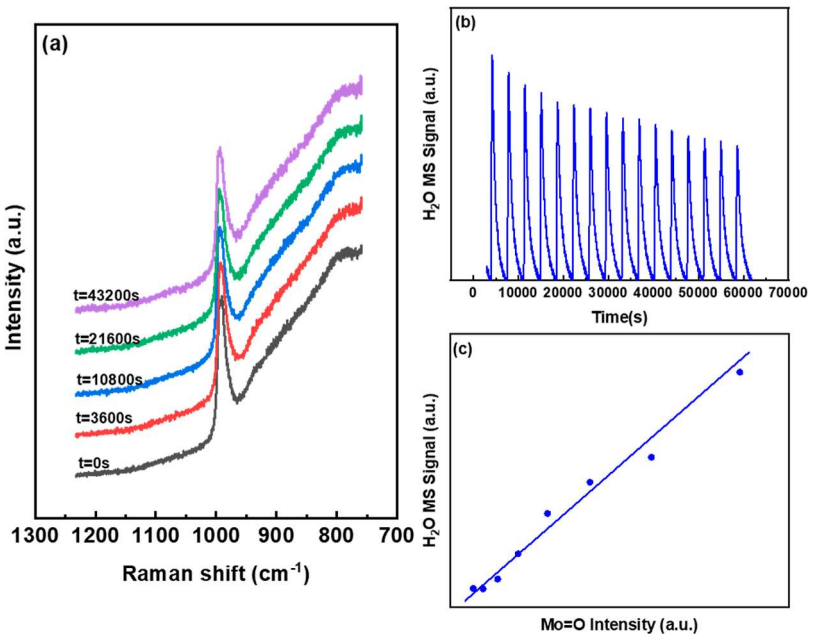


**Figure 6.** (a) Operando Raman spectra under a $H_2$ pulse at 600 °C. (b) $H_2O$ mass spectrum signal. (c) Correlation between the molybdenyl oxygen signal and $H_2O$ formation signal from the mass spectrum.

analysis showed that the 996 $cm^{-1}$ band, under $^{18}O_2$ flow, was not similarly recovered as the rest of the components. This implies that the new emergence of the band around ~940 $cm^{-1}$, especially at the early stage of the substitution, mainly arises from the oxygen replacement of the Mo═O functionality of the species, which corresponds to the 996 $cm^{-1}$ component. In other words, different $MoO_x$ structural species, signified by different component Mo═O peaks around 1000 $cm^{-1}$, show different reducibilities. Consequently, as more redox cycles take place, the substitution of free Mo═O units from species with different reducibilities occurred at different rates, resulting in a progressive red shift of the Mo═$^{16}$O band. This red shift has also been observed in previous studies of molybdena catalysts supported on $TiO_2$, $Al_2O_3$, and $ZrO_2$ with higher loadings than this study.[47,48] However, it was hypothesized that the shift was caused by the consecutive isotopic exchange steps.[48] The hypothesis suggests that the substitution order begins with the reduction and substitution of neighboring oxygen sites (Mo−O−Mo/Mo-O-*Support*), leading to the slight elongation of the terminal bond, thus subsequently causing the removal and substitution of terminal oxygen.

To shed more light on the reactivity of molybdenyl under reduction conditions, we applied an operando Raman spectrokinetic approach on the MoTi4 catalyst where reduction with $H_2$ took place in a pulse mode while collecting Raman spectra together with mass spectrometry data for the $H_2O$ produced (Figure 6). Considering that the overall reduction process was conducted in pulse mode, the total $H_2$ flux throughout the experiment is much lower than that used in the flow process, as reported in Figures 4 and 5. The results summarized in Figure 6 show that at the very early stage of the reduction process, the $H_2$ consumption and $H_2O$ formation show a linear correlation with the intensity reduction of the molybdenyl oxygen band. This correlation implies that Mo═O is the primary source consuming $H_2$ and forming $H_2O$ when the overall oxidative state of the material is high. In other words, oxygen atoms that are attached to Mo═O can be reduced earlier than those in Mo−O−X. It is noteworthy that potential intermediate steps between the fully oxidative state and oxygen removal may exist, yet remain elusive to Raman spectroscopy due to their transitional nature and unstable products. Fully capturing these transitional steps would necessitate more advanced and transient spectroscopic techniques such SITKA-DRIFTS or spectroscopic methods under Modulation Excitation methodology. Consequently, the above analysis implies that the slight red shift of the Mo═O band, during the isotopic substitution process as mentioned above, might very well be contributed by the change in the percentage of Mo═O component peaks, caused by the different reducibility between Mo═O from different structures.

Computational analysis was also employed to further assist with the vibrational assignments of the various molybdena species. Several monomeric, dimeric, and trimeric structural models were considered, and their optimized structures are shown in Table S3. The frequencies for the selected vibrational modes are listed in Table 1. Across all models, substituting $^{18}O$

**Table 1. Calculated Frequencies ($cm^{-1}$) for Different $MoO_x$/$TiO_2$ Structures**

| | Mo═O | Mo−O−Mo $\nu_{as}$ | Mo−O−Ti $\nu_{as}$ |
|---|---|---|---|
| $Mo^{(VI)}O_5$ | 992 | | 908 |
| $Mo^{(VI)}O_5$ Mo═$^{18}O$ | 954 | | 907 |
| $Mo^{(V)}O_4$ | 983 | | 888, 875 |
| $Mo^{(V)}O_4$ Mo═$^{18}O$ | 935 | | 889, 877 |
| $Mo^{(V)}O_4$ all $^{18}O$ | 933 | | 867, 860 |
| dimer $Mo^{(VI)}$ | 1001, 994 | 768 | 925, 913 |
| dimer $Mo^{(VI)}$ Mo═$^{18}O$ | 996, 953 | | |
| dimer $Mo^{(VI)}$ Mo−$^{18}$O−Mo | 1001, 994 | 728 | 925, 913 |
| dimer $Mo^{(VI)}$ Mo−$^{18}$O−Ti | 1000, 994 | 768 | 918, 894 |
| linear trimer $Mo^{(VI)}$ | 1012, 1005, 990 | 738 | 881, 879 |
| cyclic trimer[a] | 996, 989 | 864, 850−830 | 864, 850−830 |

[a]Mo−O−Mo and Mo−O−Ti are coupled.



https://doi.org/10.1021/acs.jpcc.4c02018
J. Phys. Chem. C 2024, 128, 9169−9181

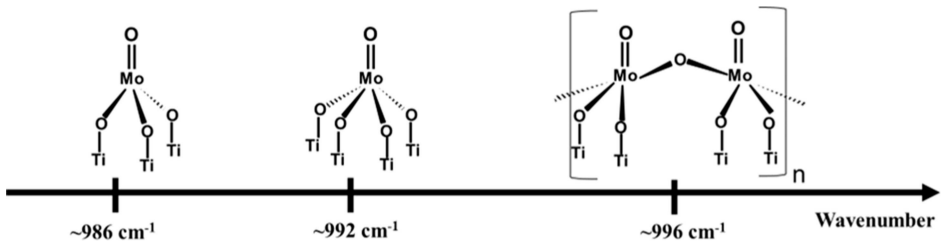


**Figure 7.** Schematic assignments of the Mo═O vibration of different Mo oxo structures for MoTi samples.

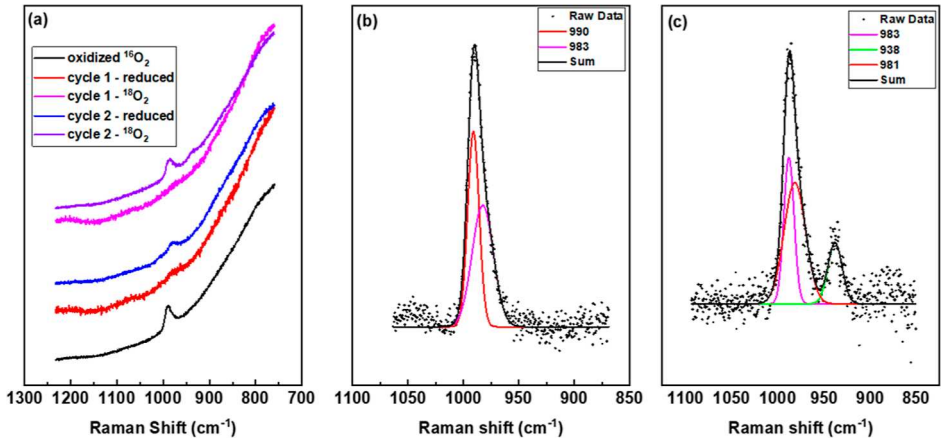


**Figure 8.** (a) Raman spectra of MoCeTi9 during different isotopic substitution cycles at 600 °C. (b,c) Deconvolution analysis of the terminal oxygen band for MoTi9 under air flow and under $^{18}O_2$ flow, respectively.

for the molybdenyl oxygen resulted in a relative shift of 38−50 $cm^{-1}$. It is important to note that the formally reduced $MoO_4$ structure experiences a shift of 10 $cm^{-1}$ greater than that of the fully oxidized $MoO_5$ structure. In the oligomeric, dimeric, or cyclic form, for instance, the model suggested two vibrational modes, one at around 1001 $cm^{-1}$ (in-phase stretching) and the other one at 994 $cm^{-1}$ (out-of-phase stretching), close to that of monomeric $MoO_5$. It is interesting that when the anchoring or bridging oxygen of a dimer is replaced by $^{18}O$, the models predict an insignificant change in the Mo═O vibrational frequencies. These results support our argument that the slight shift in the enveloping Mo═O band can be caused by a change in the distribution of the remaining Mo═O component peaks from distinct structures. Experimental analysis for both MoTi and MoCeTi samples suggests that at least three Gaussian component peaks under Mo═O exist and should be accounted for by DFT calculations. Furthermore, the experimental results also hint that the Mo═O peak, which is associated with polymeric species, should locate at a higher frequency than the monomers. It is noteworthy that previous DFT studies[63,64] also conclude the existence of stable $Mo^{(V)}$ and $Mo^{(VI)}$ species on the $TiO_2$ surface even though the $Mo^{(VI)}$ structures are embedded in polymeric forms. In this study, it is found that despite being much more distorted, the structure of monomeric $Mo^{(VI)}$ has a Mo═O vibration frequency well in line with one of the component peaks under Mo═O, observed experimentally. Last but not least, the use of advanced spectroscopic techniques, such as from High Field 51 V MAS NMR,[101,102] have prior revealed diverse vanadium surface species on $TiO_2$, with molecular structure variations possibly linked also to anchoring on distinct exposed facets. Such molecular variations could potentially be present in our system, thus inducing a highly complex surface. Laser micro-Raman spectroscopy exposes challenges in distinguishing all possible species due to the spot size of the laser, impacting the overall Raman spectrum's interpretation. Moreover, some species present at very low concentrations may not be detected due to the sensitivity of the measurements. While our approach prioritizes minimal Gaussian peaks with physical meaning, future research integrating visible as well as UV resonance Raman data with advanced spectroscopic techniques like extended X-ray absorption fine structure (EXAFS), X-ray absorption near-edge spectroscopy, and solid-state nuclear magnetic resonance (NMR) will be needed to shed more light on the competition of multiple adsorbed species on the surface of complex oxides. Matching the spectral behaviors of supported molybdena on $TiO_2$ synthesized in this work by the EDF method with the isotopic exchange experiments and computational analysis, we illustrate the possible configurations along with their M═O frequencies in Figure 7.

**Isotopic Exchange Experiments and Surface Structure Confirmation of $(MoO_x)_n$ on $CeO_2$−$TiO_2$.** Isotopic substitution experiments were also performed over the $(MoO_x)_n$ catalysts supported on $CeO_2$−$TiO_2$, and the relevant results are shown in Figures 8−10. We summarize below a few distinct features in the collected Raman spectra:

(i) $^{18}O$ substitution leads to the emergence of only one new peak for both MoCeTi9 and MoCeTi4 samples at 938 and 940 $cm^{-1}$, respectively, signifying the presence of mono-oxo species.

(ii) With consecutive redox cycles, the enveloping unsubstituted Mo═$^{16}O$ band progressively red shifts for both MoCeTi9 and MoCeTi4, indicating, as in the case of pure $TiO_2$, the presence of $(MoO_x)_n$ species with different reducibilities.

(iii) 18O substitution into Mo−O−X causes the appearance of a low energy component peak at ~880 cm−1. The



https://doi.org/10.1021/acs.jpcc.4c02018
J. Phys. Chem. C 2024, 128, 9169−9181

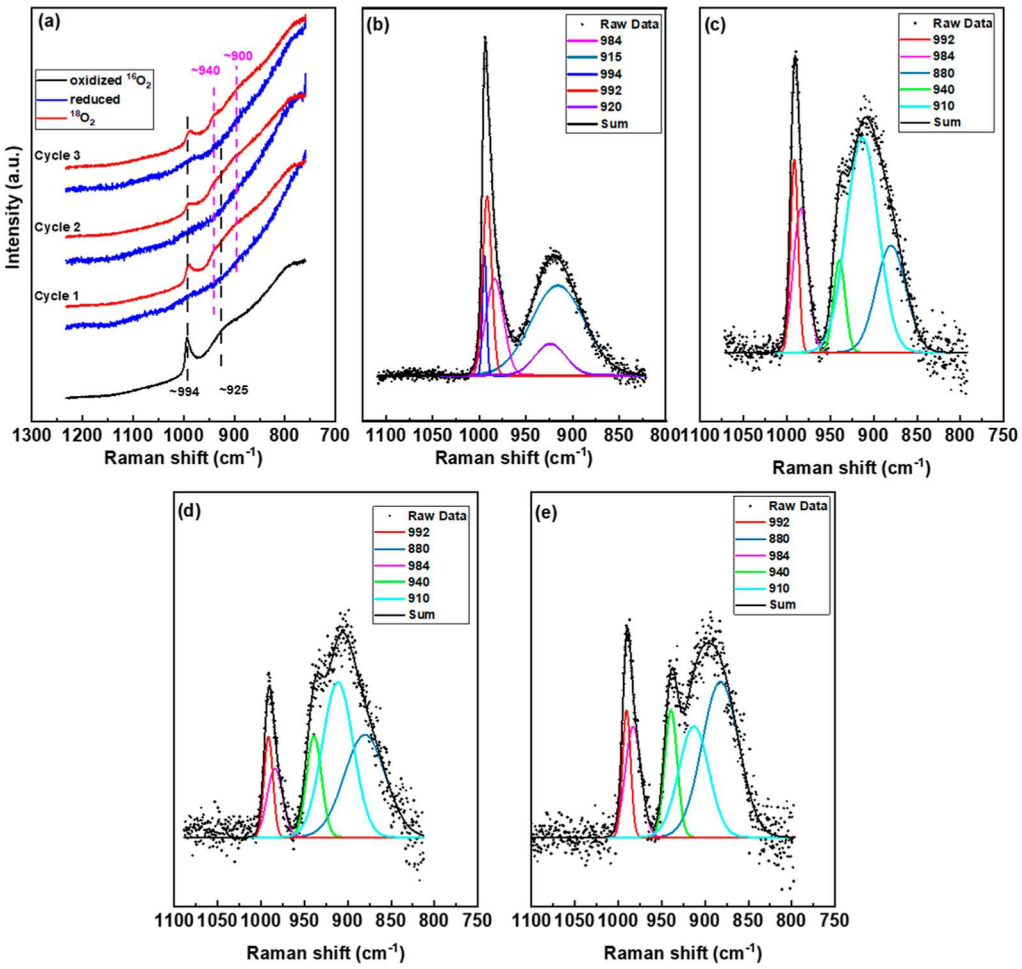


**Figure 9.** (a) Raman spectra of MoCeTi4 at different isotopic substitution cycles at 600 °C. (b,c) Deconvolution analysis of the terminal oxygen band for MoTi4 under air flow and under $^{18}O_2$ flow, respectively.

appearance of this new peak is responsible for the overall enhancement and broadening of the spectral envelop, initially centered at ∼900 cm−1.

(iv) Upon shorter exposure of the MoCeTi4 sample to $H_2$, we observe a significant decrease in the intensity of Mo═O, while the overall Mo−O−X (∼900 cm$^{-1}$) appears to experience negligible change.

(v) After several redox cycles (with short reduction period), the spectral analysis for the reoxidation process by $^{18}O_2$ shows that besides the appearance of the 940 cm$^{-1}$ peak (Mo═$^{18}$O), one of the Mo−O−X components shifts to lower frequencies, while the other one remains at a fixed position.

(vi) Similar to the case of pure $TiO_2$ samples, the band pertaining to Mo═$^{16}$O demonstrates intensity recovery when the materials are exposed to $^{18}O_2$ in all isotopic experiments.

Experimentally, under the $^{16}O_2$ flow, the deconvolution analysis recognizes an energy gap of 5 cm$^{-1}$ between component peaks at ∼915 and ∼920 cm$^{-1}$. Meanwhile, under $^{18}O_2$ conditions, the two component peaks under the Mo−O−X band, ∼910 and ∼880 cm$^{-1}$, are widely separated by ∼30 cm$^{-1}$. Such strong perturbation in component peak positions during the isotopic substitution process helps increase the reliability of identifying at least two component peaks in the Mo−O−X band region. Also, when the terminal oxygen is purportedly reduced to substitute with $^{18}$O, the absence of the ∼880 cm$^{-1}$ band coincides with the persistence of the peak at ∼920 cm$^{-1}$ while the appearance of the ∼910 cm$^{-1}$ peak aligns with the absence of the peak at ∼915 cm$^{-1}$. This suggests that the $^{18}$O substitution in the 915 cm$^{-1}$ and 920 cm$^{-1}$ peaks corresponds to the generation of the peaks at ∼910 and 880 cm$^{-1}$, respectively. The remarkably distinguishing spectral behaviors of the two component peaks under Mo−O−X pertain to either two oxide structures or two bonds (Mo−O−X and Mo−O−X′). At this point, computational results, shown in Table 1, can bring more clarity to species identification. DFT analysis indicates that an isolated $MoO_5$ structure exhibits mainly only one mode for the Mo−O−Ti vibration, which does not agree with the experimental observation. While an isolated $MoO_4$ structure shows two modes of vibration in the range of 850−950 cm$^{-1}$, the spread of these two vibrational modes slightly shrinks upon $^{18}$O substitution, from ∼13 to 12 cm$^{-1}$ (or 7 cm$^{-1}$ in the case when all oxygen sites are replaced). These features, obtained from computational analysis, confirm the absence of monomeric $MoO_x$ on the surface of MoCeTi4. In contrast, dimeric molybdena behaves very differently. Upon $^{18}$O substitution, the two modes of the Mo−O−Ti vibration considerably increase their positional spread from ∼12 to ∼24 cm$^{-1}$. This behavior resembles the spectroscopic trend recorded from the experiments. Such an agreement not only confirms the presence of polymeric structures for the MoCeTi4 case but also suggests



https://doi.org/10.1021/acs.jpcc.4c02018
J. Phys. Chem. C 2024, 128, 9169−9181

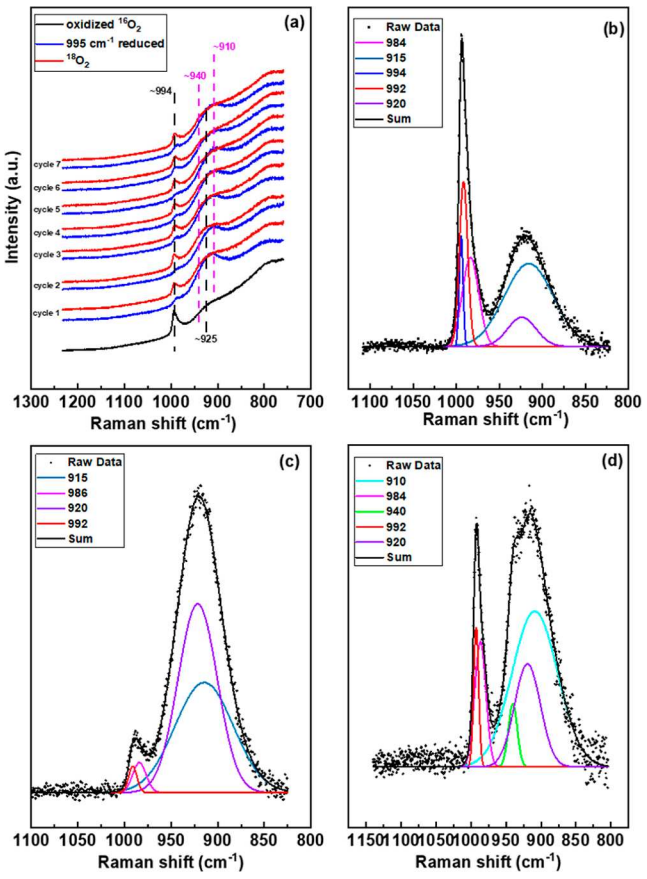


**Figure 10.** (a) Raman spectra of MoCeTi4 at different isotopic substitution cycles at 600 °C after the terminal oxygen band is mostly reduced. (b–d) Deconvolution analysis of the terminal oxygen band for MoTi9 under air flow, $H_2$ reduction condition, and $^{18}O_2$ flow, respectively.

that the broad band at ~900 cm$^{-1}$ of polymeric molybdena structures envelops at least two different types of vibrational modes of anchoring oxygens (Mo−O−Ti). The rise of different modes of anchoring oxygen, Mo−O−Ti, might be caused by the strong distortion of these bonds when a bridging bond between oxo structures is formed.

The recovery of the Raman signal in the Mo═$^{16}$O band under $^{18}O_2$ flow for all samples of both supported Mo on pure anatase $TiO_2$ and $CeO_2$−$TiO_2$ could be observed even in the experiment, when the materials were highly reduced. The absence of the $^{16}$O source in the atmosphere suggests that the presence of the Mo═$^{16}$O band bcould be due to the $^{16}$O coming from the material surface. We hypothesize that during the reduction phase, besides the removal of terminal oxygen, some anchoring bonds between oxygen and support/Mo, Mo-$^{16}$O-support/Mo, could also be broken, visually demonstrated in Figure 11. These remaining $^{16}$O might compete with newly added $^{18}$O from the gas phase to become the next terminal oxygen in the oxidation phase. The oxygen restructuring process seems to preferably occur at specific oxygen sites because when the molybdenyl is targeted for isotopic oxygen substitution, the peak at ~920 cm$^{-1}$ experiences a negligible change as compared to the ~915 cm$^{-1}$ peak. It is worth mentioning that the recovery of Mo═$^{16}$O under $^{18}O_2$ flow was previously observed for other systems such as supported vanadium on ceria.[103] Based on the high reducibility of ceria and strong mobility of its oxygen, a simple oxygen transfer from the support to the active vanadium site was suggested as the main cause of the Mo═$^{16}$O signal. In our isotopic experiment, the material is flushed with inert gas for a long period of time before spectral collection after reduction phase. During this process, there is no recovery of the Mo═$^{16}$O signal. The absence of such recovery partially negates the hypothesis of oxygen transfer. Even if one argues that the oxygen transfer only occurs under an oxidation driving force, which is $^{16}O_2$ or $^{18}O_2$ flow, the hypothesis of oxygen transfer can still be negated by the fact that oxygen transfer has significantly slower kinetics as compared to that of reoxidation of material by the abundant $O_2$ gas present in the atmosphere. In other words, in the presence of gaseous $^{18}O_2$, if surface $^{16}$O transfer is the main cause of Mo═$^{16}$O, the signal of Mo═$^{18}$O will be expected to be remarkably stronger than that of Mo═$^{16}$O in the first exchange cycle and the recovery of Mo═$^{16}$O will be expected to occur at a much slower pace than the appearance of Mo═$^{18}$O. On the contrary, the signal of Mo═$^{18}$O is very weak in the first few exchange cycles and the emergence of Mo═$^{18}$O in each cycle occurs simultaneously as the recovery of Mo═$^{16}$O. Future research efforts to fully resolve the mechanistic details of such structural transformation will require the combination of multiple advanced spectroscopic techniques such as operando Raman, X-ray photoelectron spectroscopy, and EXAFS in order to couple vibrational insights with oxidative states and coordination information on the same structures under identical reaction conditions.

## CONCLUSIONS

A transient operando Raman spectroscopy framework, exemplified by the case of supported molybdenum oxide on

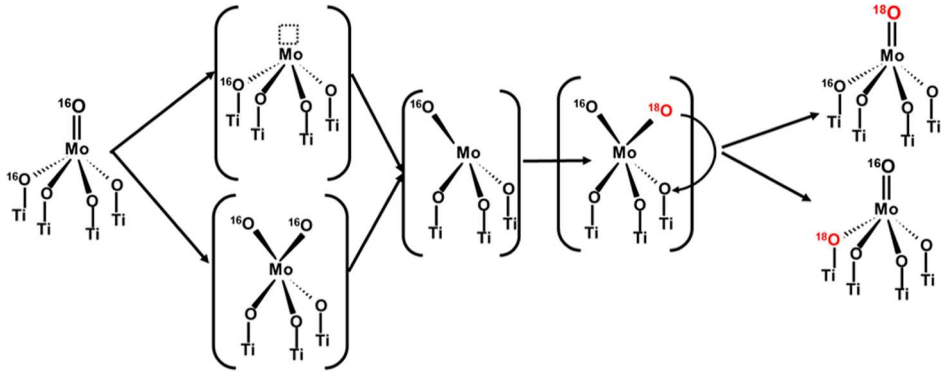


**Figure 11.** Schematics of the restructuring process of oxo Mo sites during redox cycles.



https://doi.org/10.1021/acs.jpcc.4c02018
J. Phys. Chem. C 2024, 128, 9169−9181

pure anatase $TiO_2$ and mixed $CeO_2$−$TiO_2$, is presented in this work. Starting from a well-established and well-controlled EDF synthesis technique, it is pointed out that pH manipulation leads to different distributions of molybdenum surface structures. As the pH during the synthesis decreases, the overall loading of deposited molybdenum becomes higher but still stays below the monolayer coverage. Low pH synthesis also induces the formation of more 6-coordination oxo-configurations on the surface and oligomeric structures on $CeO_2$−$TiO_2$, while higher pH synthesis restricts the formation of a dominant monomeric structure. The combination of Raman operando $H_2$ pulse and $^{18}O/^{16}O$ isotope exchange reveals that the structure of supported Mo on pure anatase $TiO_2$ and on mixed $CeO_2$−$TiO_2$ pertains mainly to mono-oxo. Among terminal oxygens that pertain to different oxo-structures, those associated with higher wavenumber vibrational mode appear to be reduced and substituted first, causing a slight red shift in the enveloping Mo═$^{16}$O band. Distinguishing spectral behaviors of two component peaks under the band around ∼900 $cm^{-1}$ confirms the existence of two distinct vibrational modes of different anchoring Mo-O-*Support* bonds. Some recovery of the Mo═$^{16}$O signal during the reoxidation phase with $^{18}O_2$ flow, observed for all materials, demonstrated the possible restructuring process during the redox cycles, in which oxygens from Mo−O−X bonds can swap around and become a Mo═O.

## ■ ASSOCIATED CONTENT

### Supporting Information

The Supporting Information is available free of charge at https://pubs.acs.org/doi/10.1021/acs.jpcc.4c02018.

XRF analysis of $MoO_x$ samples, BET measurements of support samples, optimized structures of $MoO_x$ supported on $TiO_2$, and Raman spectra of support samples at room and elevated temperatures (PDF)

## ■ AUTHOR INFORMATION


### Corresponding Author

**George Tsilomelekis** − *Department of Chemical and Biochemical Engineering, Rutgers, the State University of New Jersey, Piscataway, New Jersey 08854, United States;* orcid.org/0000-0002-0435-8216; Email: g.tsilo@rutgers.edu

### Authors

**Thu D. Nguyen** − *Department of Chemical and Biochemical Engineering, Rutgers, the State University of New Jersey, Piscataway, New Jersey 08854, United States*

**Alfred Worrad** − *University of Delaware, Newark, Delaware 19716, United States;* orcid.org/0000-0002-5868-931X

**Dhanush Thirulogachandar** − *Department of Chemical and Biochemical Engineering, Rutgers, the State University of New Jersey, Piscataway, New Jersey 08854, United States*

**Fuat E. Celik** − *Department of Chemical and Biochemical Engineering, Rutgers, the State University of New Jersey, Piscataway, New Jersey 08854, United States;* orcid.org/0000-0002-5891-6375

**Stavros Caratzoulas** − *University of Delaware, Newark, Delaware 19716, United States;* orcid.org/0000-0001-9599-4199

Complete contact information is available at: https://pubs.acs.org/10.1021/acs.jpcc.4c02018


### Notes

The authors declare no competing financial interest.

## ■ ACKNOWLEDGMENTS

This work was conducted with funding from the RAPID manufacturing institute, supported by the Department of Energy (DOE) Advanced Manufacturing Office (AMO), award number DE-EE0007888. Part of this work was also funded in part by Rutgers, The State University of New Jersey, and the National Science Foundation Award #1751683.

## ■ REFERENCES


(1) Brookes, C.; Wells, P. P.; Cibin, G.; Dimitratos, N.; Jones, W.; Morgan, D. J.; Bowker, M. Molybdenum Oxide on Fe2O3 Core-Shell Catalysts: Probing the Nature of the Structural Motifs Responsible for Methanol Oxidation Catalysis. *ACS Catal.* **2014**, *4* (1), 243−250.

(2) Chakrabarti, A.; Wachs, I. E. Molecular Structure−Reactivity Relationships for Olefin Metathesis by $Al_2O_3$-Supported Surface $MoO_x$ Sites. *ACS Catal.* **2018**, *8* (2), 949−959.

(3) Cheng, E.; Notestein, J. Catalytic dehydrogenation of isobutane over supported MoOx/K-Al2O3. *J. Catal.* **2021**, *397*, 212−222.

(4) Gao, J.; Zheng, Y.; Jehng, J.-M.; Tang, Y.; Wachs, I. E.; Podkolzin, S. G. Identification of molybdenum oxide nanostructures on zeolites for natural gas conversion. *Science* **2015**, *348* (6235), 686−690.

(5) Goelden, V.; Linke, D.; Kondratenko, E. V. Investigation of the Enhancing Effect of Solid Cocatalysts on Propene Formation in Ethene/*trans*-2-Butene Metathesis over $MoO_x/SiO_2$−$Al_2O_3$. *ACS Catal.* **2015**, *5* (12), 7437−7445.

(6) Kiani, D.; Sourav, S.; Tang, Y.; Baltrusaitis, J.; Wachs, I. E. Methane activation by ZSM-5-supported transition metal centers. *Chem. Soc. Rev.* **2021**, *50* (2), 1251−1268.

(7) Lwin, S.; Wachs, I. E. Olefin Metathesis by Supported Metal Oxide Catalysts. *ACS Catal.* **2014**, *4* (8), 2505−2520.

(8) Matam, S. K.; Moffat, C.; Hellier, P.; Bowker, M.; Silverwood, I. P.; Catlow, C. R. A.; Jackson, S. D.; Craswell, J.; Wells, P. P.; Parker, S. F.; et al. Investigation of MoOx/Al2O3 under Cyclic Operation for Oxidative and Non-Oxidative Dehydrogenation of Propane. *Catalysts* **2020**, *10*, 1370.

(9) Mouat, A. R.; Lohr, T. L.; Wegener, E. C.; Miller, J. T.; Delferro, M.; Stair, P. C.; Marks, T. J. Reactivity of a Carbon-Supported Single-Site Molybdenum Dioxo Catalyst for Biodiesel Synthesis. *ACS Catal.* **2016**, *6* (10), 6762−6769.

(10) Noh, H.; Cui, Y.; Peters, A. W.; Pahls, D. R.; Ortuño, M. A.; Vermeulen, N. A.; Cramer, C. J.; Gagliardi, L.; Hupp, J. T.; Farha, O. K. An Exceptionally Stable Metal-Organic Framework Supported Molybdenum(VI) Oxide Catalyst for Cyclohexene Epoxidation. *J. Am. Chem. Soc.* **2016**, *138* (44), 14720−14726.

(11) Novotný, P.; Yusuf, S.; Li, F.; Lamb, H. H. MoO3/Al2O3 catalysts for chemical-looping oxidative dehydrogenation of ethane. *J. Chem. Phys.* **2020**, *152* (4), 044713.

(12) Otroshchenko, T.; Zhang, Q.; Kondratenko, E. V. Enhancing Propene Formation in the Metathesis of Ethylene with 2-Butene at Close to Room Temperature over $MoO_x/SiO_2$ through Support Promotion with P, Cl, or S. *ACS Catal.* **2021**, *11* (22), 14159−14167.

(13) Qin, S.; Li, J.; Long, J.; Yang, X.; Miao, P. Promotion Effect of Cerium on Mo/Al2O3 Catalyst for Methanation. *Appl. Catal., A* **2020**, *598*, 117559.

(14) Rasmussen, M. J.; Najmi, S.; Innocenti, G.; Medford, A. J.; Sievers, C.; Medlin, J. W. Supported molybdenum oxides for the aldol condensation reaction of acetaldehyde. *J. Catal.* **2022**, *408*, 216−226.

(15) Shetty, M.; Murugappan, K.; Prasomsri, T.; Green, W. H.; Román-Leshkov, Y. Reactivity and stability investigation of supported molybdenum oxide catalysts for the hydrodeoxygenation (HDO) of m-cresol. *J. Catal.* **2015**, *331*, 86−97.

(16) Sudarsanam, P.; Gupta, N. K.; Mallesham, B.; Singh, N.; Kalbande, P. N.; Reddy, B. M.; Sels, B. F. Supported $MoO_x$ and $WO_x$ Solid Acids for Biomass Valorization: Interplay of Coordination

Chemistry, Acidity, and Catalysis. *ACS Catal.* **2021**, *11* (21), 13603−13648.
(17) Teh, L. P.; Setiabudi, H. D.; Sidik, S. M.; Annuar, N. H. R.; Jalil, A. A. Synergic role of platinum (Pt) and molybdenum trioxide (MoO3) promoted HBEA zeolite towards n-heptane isomerization. *Mater. Chem. Phys.* **2021**, *263*, 124406.
(18) Toyao, T.; Kayamori, S.; Maeno, Z.; Siddiki, S. M. A. H.; Shimizu, K.-i. Heterogeneous Pt and $MoO_x$ Co-Loaded $TiO_2$ Catalysts for Low-Temperature $CO_2$ Hydrogenation To Form $CH_3OH$. *ACS Catal.* **2019**, *9* (9), 8187−8196.
(19) Yamamoto, K.; Chan, K. W.; Mougel, V.; Nagae, H.; Tsurugi, H.; Safonova, O. V.; Mashima, K.; Copéret, C. Silica-supported isolated molybdenum di-oxo species: formation and activation with organosilicon agent for olefin metathesis. *Chem. Commun.* **2018**, *54* (32), 3989−3992.
(20) Yang, F.; Libretto, N. J.; Komarneni, M. R.; Zhou, W.; Miller, J. T.; Zhu, X.; Resasco, D. E. Enhancement of *m*-Cresol Hydrodeoxygenation Selectivity on Ni Catalysts by Surface Decoration of $MoO_x$ Species. *ACS Catal.* **2019**, *9* (9), 7791−7800.
(21) Yao, R.; Herrera, J. E.; Chen, L.; Chin, Y.-H. C. Generalized Mechanistic Framework for Ethane Dehydrogenation and Oxidative Dehydrogenation on Molybdenum Oxide Catalysts. *ACS Catal.* **2020**, *10* (12), 6952−6968.
(22) Yao, R.; Pinals, J.; Dorakhan, R.; Herrera, J. E.; Zhang, M.; Deshlahra, P.; Chin, Y.-H. C. Cobalt-Molybdenum Oxides for Effective Coupling of Ethane Activation and Carbon Dioxide Reduction Catalysis. *ACS Catal.* **2022**, *12* (19), 12227−12245.
(23) Zhang, B.; Xiang, S.; Frenkel, A. I.; Wachs, I. E. Molecular Design of Supported $MoO_x$ Catalysts with Surface $TaO_x$ Promotion for Olefin Metathesis. *ACS Catal.* **2022**, *12* (5), 3226−3237.
(24) Zhang, H.; Gao, X.; Gong, B.; Shao, S.; Tu, C.; Pan, J.; Wang, Y.; Dai, Q.; Guo, Y.; Wang, X. Catalytic combustion of CVOCs over MoOx/CeO2 catalysts. *Appl. Catal., B* **2022**, *310*, 121240.
(25) Liu, S.; Dong, Q.; Ohnishi, R.; Ichikawa, M. Remarkable non-oxidative conversion of methane to naphthalene and benzene on Co and Fe modified Mo/HZSM-5 catalysts. *Chem. Commun.* **1997**, No. 15, 1455−1456.
(26) Nguyen, T. D.; Zheng, W.; Celik, F. E.; Tsilomelekis, G. $CO_2$-assisted ethane oxidative dehydrogenation over $MoO_x$ catalysts supported on reducible $CeO_2$−$TiO_2$. *Catal. Sci. Technol.* **2021**, *11* (17), 5791−5801.
(27) Yang, Y.; Peng, Z.; Zhao, H.; Wang, E.; Li, C. Ce-Modified Mo/γ-Al2O3 Catalysts for Production of Elemental Sulfur through Reducing SO2. *Ind. Eng. Chem. Res.* **2021**, *60* (44), 15942−15950.
(28) Yu, J.; Luo, B.; Wang, S.; Wu, K.; Tao, Y.; Chu, S.; Zhang, H. Enhanced aromatic yield from catalytic pyrolysis of pine wood via ultrasonic assisted Mo modified HZSM-5. *Biomass Bioenergy* **2023**, *172*, 106769.
(29) Lee, E. L.; Wachs, I. E. In Situ Raman Spectroscopy of SiO2-Supported Transition Metal Oxide Catalysts: An Isotopic 18O-16O Exchange Study. *J. Phys. Chem. C* **2008**, *112* (16), 6487−6498.
(30) Fievez, T.; Geerlings, P.; Weckhuysen, B. M.; De Proft, F. Using DFT in search for support effects during methanol oxidation on supported molybdenum oxides. *ChemPhysChem* **2011**, *12* (17), 3281−3290.
(31) Handzlik, J.; Ogonowski, J. Structure of Isolated Molybdenum-(VI) and Molybdenum(IV) Oxide Species on Silica: Periodic and Cluster DFT Studies. *J. Phys. Chem. C* **2012**, *116* (9), 5571−5584.
(32) Handzlik, J. DFT study of molybdena-silica system - A selection of density functionals based on their performance in thermochemistry of molybdenum compounds. *Chem. Phys. Lett.* **2009**, *469* (1−3), 140−144.
(33) Gregoriades, L. J.; Döbler, J.; Sauer, J. Oxidation of Methanol to Formaldehyde on Silica-Supported Molybdena: Density Functional Theory Study on Models of Mononuclear Sites. *J. Phys. Chem. C* **2010**, *114* (7), 2967−2979.
(34) Guo, C. S.; Hermann, K.; Hävecker, M.; Thielemann, J. P.; Kube, P.; Gregoriades, L. J.; Trunschke, A.; Sauer, J.; Schlögl, R. Structural Analysis of Silica-Supported Molybdena Based on X-ray Spectroscopy: Quantum Theory and Experiment. *J. Phys. Chem. C* **2011**, *115* (31), 15449−15458.
(35) Lee, E. L.; Wachs, I. E. In Situ Spectroscopic Investigation of the Molecular and Electronic Structures of SiO2 Supported Surface Metal Oxides. *J. Phys. Chem. C* **2007**, *111* (39), 14410−14425.
(36) Lal Bose, A.; Ramteke, S.; Deo, G.; Agarwal, V. Structures and reactivity of monomeric MoOx moieties supported on ZrO2 (111) slab: A DFT study. *J. Catal.* **2024**, *429*, 115267.
(37) Magg, N.; Immaraporn, B.; Giorgi, J. B.; Schroeder, T.; Bäumer, M.; Döbler, J.; Wu, Z.; Kondratenko, E.; Cherian, M.; Baerns, M.; et al. Vibrational spectra of alumina- and silica-supported Vanadia revisited: An experimental and theoretical model catalyst study. *J. Catal.* **2004**, *226* (1), 88−100.
(38) Chary, K. V. R.; Reddy, K. R.; Kishan, G.; Niemantsverdriet, J. W.; Mestl, G. Structure and catalytic properties of molybdenum oxide catalysts supported on zirconia. *J. Catal.* **2004**, *226* (2), 283−291.
(39) Busca, G. Differentiation of mono-oxo and polyoxo and of monomeric and polymeric vanadate, molybdate and tungstate species in metal oxide catalysts by IR and Raman spectroscopy. *J. Raman Spectrosc.* **2002**, *33* (5), 348−358.
(40) Huang, C.; Feng, Z.; Pei, F.; Fu, A.; Qu, B.; Chen, X.; Fang, X.; Kang, H.; Cui, J. Understanding Protection Mechanisms of Graphene-Encapsulated Silicon Anodes with Operando Raman Spectroscopy. *ACS Appl. Mater. Interfaces* **2020**, *12* (31), 35532−35541.
(41) Jiang, X.; Lis, B. M.; Wu, Y.; Wachs, I. E.; Wu, Z. Effect of the Molecular Structure of Surface Vanadia on Activity and Regenerability of $VO_x/In_2O_3$ Catalysts for $CO_2$-Assisted Oxidative Dehydrogenation of Propane. *J. Phys. Chem. C* **2023**, *127* (13), 6311−6320.
(42) Kentri, T.; Trimpalis, A.; Misa, A.; Kordouli, E.; Ramantani, T.; Boghosian, S. Rethinking the molecular structures of $W^{VI}O_x$ sites dispersed on titania: distinct mono-oxo configurations at 430 °C and temperature-dependent transformations. *Dalton Trans.* **2022**, *51* (19), 7455−7475.
(43) Moncada, J.; Adams, W. R.; Thakur, R.; Julin, M.; Carrero, C. A. Developing a Raman Spectrokinetic Approach To Gain Insights into the Structure-Reactivity Relationship of Supported Metal Oxide Catalysts. *ACS Catal.* **2018**, *8* (10), 8976−8986.
(44) Samek, I. A.; Bobbitt, N. S.; Snurr, R. Q.; Stair, P. C. Interactions of $VO_x$ Species with Amorphous $TiO_2$ Domains on ALD-Derived Alumina-Supported Materials. *J. Phys. Chem. C* **2019**, *123* (13), 7988−7999.
(45) Schumacher, L.; Hess, C. The active role of the support in propane ODH over VOx/CeO2 catalysts studied using multiple operando spectroscopies. *J. Catal.* **2021**, *398*, 29−43.
(46) Song, J.; Impeng, S.; Zhang, J.; Deng, J.; Zhang, D. Elucidating the sensitivity of vanadyl species to water over V2O5/TiO2 catalysts for NOx abatement via operando Raman spectroscopy. *J. Catal.* **2022**, *416*, 198−208.
(47) Tsilomelekis, G.; Boghosian, S. Structural and vibrational properties of molybdena catalysts supported on alumina and zirconia studied by in situ Raman and FTIR spectroscopies combined with 18O/16O isotopic substitution. *Catal. Today* **2010**, *158* (1−2), 146−155.
(48) Tsilomelekis, G.; Boghosian, S. On the configuration, molecular structure and vibrational properties of MoOx sites on alumina, zirconia, titania and silica. *Catal. Sci. Technol.* **2013**, *3* (8), 1869−1888.
(49) Wachs, I. E.; Roberts, C. A. Monitoring surface metal oxide catalytic active sites with Raman spectroscopy. *Chem. Soc. Rev.* **2010**, *39* (12), 5002−5017.
(50) Li, X.; Wang, S.; Li, L.; Sun, Y.; Xie, Y. Progress and Perspective for In Situ Studies of CO2 Reduction. *J. Am. Chem. Soc.* **2020**, *142* (21), jacs.0c02973.
(51) MacQueen, B.; Ruiz-Yi, B.; Royko, M.; Heyden, A.; Pagan-Torres, Y. J.; Williams, C.; Lauterbach, J. In-Situ Oxygen Isotopic Exchange Vibrational Spectroscopy of Rhenium Oxide Surface Structures on Cerium Oxide. *J. Phys. Chem. C* **2020**, *124* (13), 7174−7181.
(52) Molinari, J. E.; Wachs, I. E. Presence of Surface Vanadium Peroxo-oxo Umbrella Structures in Supported Vanadium Oxide


https://doi.org/10.1021/acs.jpcc.4c02018
J. Phys. Chem. C 2024, 128, 9169−9181

Catalysts: Fact or Fiction? *J. Am. Chem. Soc.* **2010**, *132* (36), 12559−12561.
(53) Weckhuysen, B. M.; Jehng, J.-M.; Wachs, I. E. In Situ Raman Spectroscopy of Supported Transition Metal Oxide Catalysts: 18O2−16O2 Isotopic Labeling Studies. *J. Phys. Chem. B* **2000**, *104* (31), 7382−7387.
(54) Wu, Z.; Dai, S.; Overbury, S. H. Multiwavelength Raman Spectroscopic Study of Silica-Supported Vanadium Oxide Catalysts. *J. Phys. Chem. C* **2010**, *114* (1), 412−422.
(55) Zhao, C.; Wachs, I. E. An Operando Raman, IR, and TPSR Spectroscopic Investigation of the Selective Oxidation of Propylene to Acrolein over a Model Supported Vanadium Oxide Monolayer Catalyst. *J. Phys. Chem. C* **2008**, *112* (30), 11363−11372.
(56) Chempath, S.; Zhang, Y.; Bell, A. T. DFT Studies of the Structure and Vibrational Spectra of Isolated Molybdena Species Supported on Silica. *J. Phys. Chem. C* **2007**, *111* (3), 1291−1298.
(57) Guesmi, H.; Grybos, R.; Handzlik, J.; Tielens, F. Characterization of molybdenum monomeric oxide species supported on hydroxylated silica: a DFT study. *Phys. Chem. Chem. Phys.* **2014**, *16* (34), 18253−18260.
(58) Amakawa, K.; Wang, Y.; Kröhnert, J.; Schlögl, R.; Trunschke, A. Acid sites on silica-supported molybdenum oxides probed by ammonia adsorption: Experiment and theory. *Mol. Catal.* **2019**, *478*, 110580.
(59) Handzlik, J.; Sautet, P. Structure of Isolated Molybdenum(VI) Oxide Species on γ-Alumina: A Periodic Density Functional Theory Study. *J. Phys. Chem. C* **2008**, *112* (37), 14456−14463.
(60) Handzlik, J.; Sautet, P. Structure of Dimeric Molybdenum(VI) Oxide Species on γ-Alumina: A Periodic Density Functional Theory Study. *J. Phys. Chem. C* **2010**, *114* (45), 19406−19414.
(61) Gonçalves, V. O. O.; Ciotonea, C.; Arrii-Clacens, S.; Guignard, N.; Roudaut, C.; Rousseau, J.; Clacens, J.-M.; Royer, S.; Richard, F. Effect of the support on the hydrodeoxygenation of m -cresol over molybdenum oxide based catalysts. *Appl. Catal., B* **2017**, *214*, 57−66.
(62) Tougerti, A.; Berrier, E.; Mamede, A. S.; La Fontaine, C.; Briois, V.; Joly, Y.; Payen, E.; Paul, J. F.; Cristol, S. Synergy between XANES spectroscopy and DFT to elucidate the amorphous structure of heterogeneous catalysts: TiO2-supported molybdenum oxide catalysts. *Angew. Chem., Int. Ed.* **2013**, *52* (25), 6440−6444.
(63) Asada, D.; Ikeda, T.; Muraoka, K.; Nakagawa, Y.; Tomishige, K.; Nakayama, A. Density Functional Theory Study of Deoxydehydration Reaction by TiO2-Supported Monomeric and Dimeric Molybdenum Oxide Catalysts. *J. Phys. Chem. C* **2022**, *126* (48), 20375−20387.
(64) Hamraoui, K.; Cristol, S.; Payen, E.; Paul, J.-F. Structure and reducibility of titania-supported monomeric and dimeric molybdenum oxide entities studied by DFT calculations. *J. Mol. Struct. THEOCHEM* **2009**, *903* (1−3), 73−82.
(65) Fang, J.; Bi, X.; Si, D.; Jiang, Z.; Huang, W. Spectroscopic studies of interfacial structures of CeO2-TiO2 mixed oxides. *Appl. Surf. Sci.* **2007**, *253* (22), 8952−8961.
(66) Shi, Z.; Yang, P.; Tao, F.; Zhou, R. New insight into the structure of CeO 2 -TiO 2 mixed oxides and their excellent catalytic performances for 1,2-dichloroethane oxidation. *Chem. Eng. J.* **2016**, *295*, 99−108.
(67) Georgiadou, I.; Papadopoulou, C.; Matralis, H. K.; Voyiatzis, G. A.; Lycourghiotis, A.; Kordulis, C. Preparation, Characterization, and Catalytic Properties for the SCR of NO by NH3 of V2O5/TiO2 Catalysts Prepared by Equilibrium Deposition Filtration. *J. Phys. Chem. B* **1998**, *102* (43), 8459−8468.
(68) Karakonstantis, L.; Matralis, H.; Kordulis, C.; Lycourghiotis, A. Tungsten-Oxo-Species Deposited on Alumina. II. Characterization and Catalytic Activity of Unpromoted W(vi)/γ-Al2O3Catalysts Prepared by Equilibrium Deposition Filtration (EDF) at Various pH's and Non-Dry Impregnation (NDI). *J. Catal.* **1996**, *162* (2), 306−319.
(69) Kordulis, C.; Lappas, A. A.; Fountzoula, C.; Drakaki, K.; Lycourghiotis, A.; Vasalos, I. A. NiW/γ-Al2O3 catalysts prepared by modified equilibrium deposition filtration (MEDF) and non-dry impregnation (NDI). *Appl. Catal., A* **2001**, *209* (1−2), 85−95.
(70) Spanos, N.; Matralis, H. K.; Kordulis, C.; Lycourghiotis, A. Molybdenum-oxo species deposited on titania by adsorption: Mechanism of the adsorption and characterization of the calcined samples. *J. Catal.* **1992**, *136* (2), 432−445.
(71) Spanos, N.; Vordonis, L.; Kordulis, C.; Koutsoukos, P. G.; Lycourghiotis, A. Molybdenum-oxo species deposited on alumina by adsorption: II. Regulation of the Surface MoVI Concentration by Control of the protonated Surface Hydroxyls. *J. Catal.* **1990**, *124* (2), 315−323.
(72) Spanos, N.; Vordonis, L.; Kordulis, C.; Lycourghiotis, A. Molybdenum-oxo species deposited on alumina by adsorption: I. Mechanism of the Adsorption. *J. Catal.* **1990**, *124* (2), 301−314.
(73) Tribalis, A.; Tsilomelekis, G.; Boghosian, S. Molecular structure and reactivity of titania-supported transition metal oxide catalysts synthesized by equilibrium deposition filtration for the oxidative dehydrogenation of ethane. *C.R. Chim.* **2016**, *19* (10), 1226−1236.
(74) Tsilomelekis, G.; Panagiotou, G. D.; Stathi, P.; Kalampounias, A. G.; Bourikas, K.; Kordulis, C.; Deligiannakis, Y.; Boghosian, S.; Lycourghiotis, A. Molybdena deposited on titania by equilibrium deposition filtration: structural evolution of oxo-molybdenum(vi) sites with temperature. *Phys. Chem. Chem. Phys.* **2016**, *18* (34), 23980−23989.
(75) Vakros, J.; Bourikas, K.; Kordulis, C.; Lycourghiotis, A. Influence of the Impregnation pH on the Surface Characteristics and the Catalytic Activity of the Mo/γ-Al2O3 and CoMo/γ-Al2O3 Hydrodesulfurization Catalysts Prepared by Equilibrium Deposition Filtration (EDF). *J. Phys. Chem. B* **2003**, *107* (8), 1804−1813.
(76) Vakros, J.; Lycourghiotis, A.; Voyiatzis, G. A.; Siokou, A.; Kordulis, C. CoMo/Al2O3-SiO2 catalysts prepared by co-equilibrium deposition filtration: Characterization and catalytic behavior for the hydrodesulphurization of thiophene. *Appl. Catal., B* **2010**, *96* (3−4), 496−507.
(77) Vordonis, L.; Koutsoukos, P. G.; Lycourghiotis, A. Adsorption of molybdates on doped γ-aluminas in alkaline solutions. *Colloids Surf.* **1990**, *50*, 353−361.
(78) Kuhne, T. D.; Iannuzzi, M.; Del Ben, M.; Rybkin, V. V.; Seewald, P.; Stein, F.; Laino, T.; Khaliullin, R. Z.; Schutt, O.; Schiffmann, F.; et al. CP2K: An electronic structure and molecular dynamics software package—Quickstep: Efficient and accurate electronic structure calculations. *J. Chem. Phys.* **2020**, *152* (19), 194103.
(79) VandeVondele, J.; Hutter, J. Gaussian basis sets for accurate calculations on molecular systems in gas and condensed phases. *J. Chem. Phys.* **2007**, *127* (11), 114105.
(80) Goedecker, S.; Teter, M.; Hutter, J. Separable dual-space Gaussian pseudopotentials. *Phys. Rev. B* **1996**, *54* (3), 1703−1710.
(81) Grimme, S.; Antony, J.; Ehrlich, S.; Krieg, H. A consistent and accurate ab initio parametrization of density functional dispersion correction (DFT-D) for the 94 elements H-Pu. *J. Chem. Phys.* **2010**, *132* (15), 154104.
(82) Maleki, F.; Di Liberto, G.; Pacchioni, G. pH- and Facet-Dependent Surface Chemistry of TiO2 in Aqueous Environment from First Principles. *ACS Appl. Mater. Interfaces* **2023**, *15* (8), 11216−11224.
(83) Tsilomelekis, G.; Christodoulakis, A.; Boghosian, S. Support effects on structure and activity of molybdenum oxide catalysts for the oxidative dehydrogenation of ethane. *Catal. Today* **2007**, *127* (1−4), 139−147.
(84) Tsilomelekis, G.; Boghosian, S. An operando Raman study of molecular structure and reactivity of molybdenum(vi) oxide supported on anatase for the oxidative dehydrogenation of ethane. *Phys. Chem. Chem. Phys.* **2012**, *14* (7), 2216−2228.
(85) Chua, Y. T.; Stair, P. C.; Wachs, I. E. A Comparison of Ultraviolet and Visible Raman Spectra of Supported Metal Oxide Catalysts. *J. Phys. Chem. B* **2001**, *105* (36), 8600−8606.
(86) Lai, J.-K.; Wachs, I. E. A Perspective on the Selective Catalytic Reduction (SCR) of NO with NH3 by Supported V2O5-WO3/TiO2 Catalysts. *ACS Catal.* **2018**, *8* (7), 6537−6551.
(87) Resini, C.; Montanari, T.; Busca, G.; Jehng, J.-M.; Wachs, I. E. Comparison of alcohol and alkane oxidative dehydrogenation reactions over supported vanadium oxide catalysts: in situ infrared, Raman and


https://doi.org/10.1021/acs.jpcc.4c02018
J. Phys. Chem. C 2024, 128, 9169−9181

UV-vis spectroscopic studies of surface alkoxide intermediates and of their surface chemistry. *Catal. Today* **2005**, *99* (1−2), 105−114.
(88) Bourikas, K.; Vakros, J.; Kordulis, C.; Lycourghiotis, A. Potentiometric Mass Titrations: Experimental and Theoretical Establishment of a New Technique for Determining the Point of Zero Charge (PZC) of Metal (Hydr)Oxides. *J. Phys. Chem. B* **2003**, *107* (35), 9441−9451.
(89) Vakros, J.; Kordulis, C.; Lycourghiotis, A. Potentiometric mass titrations: a quick scan for determining the point of zero charge. *Chem. Commun.* **2002**, No. 17, 1980−1981.
(90) Gu, W.; Liu, X.; Yi, P. Influence of pH and electrolyte on the deposition of cerium oxide nanoparticles on supported lipid bilayers. *Environ. Sci.: Nano* **2022**, *9* (6), 1986−1995.
(91) Gupta, K.; Bhattacharya, S.; Chattopadhyay, D.; Mukhopadhyay, A.; Biswas, H.; Dutta, J.; Ray, N. R.; Ghosh, U. C. Ceria associated manganese oxide nanoparticles: Synthesis, characterization and arsenic(V) sorption behavior. *Chem. Eng. J.* **2011**, *172* (1), 219−229.
(92) Park, J.; Regalbuto, J. R. A Simple, Accurate Determination of Oxide PZC and the Strong Buffering Effect of Oxide Surfaces at Incipient Wetness. *J. Colloid Interface Sci.* **1995**, *175* (1), 239−252.
(93) Asokan, C.; Xu, M.; Dai, S.; Pan, X.; Christopher, P. Synthesis of Atomically Dispersed Rh Catalysts on Oxide Supports via Strong Electrostatic Adsorption and Characterization by Cryogenic Infrared Spectroscopy. *J. Phys. Chem. C* **2022**, *126* (44), 18704−18715.
(94) Jiao, L.; Regalbuto, J. R. The synthesis of highly dispersed noble and base metals on silica via strong electrostatic adsorption: II. Mesoporous silica SBA-15. *J. Catal.* **2008**, *260* (2), 342−350.
(95) Martens, J. H. A.; Prins, R. Influence of pH on the preparation of monometallic rhodium and platinum, and bimetallic RhodiumPlatinum Catalysts supported on γ-Alumina. *Appl. Catal.* **1989**, *46* (1), 31−44.
(96) Miller, J. T.; Schreier, M.; Kropf, A. J.; Regalbuto, J. R. A fundamental study of platinum tetraammine impregnation of silica: 2. The effect of method of preparation, loading, and calcination temperature on (reduced) particle size. *J. Catal.* **2004**, *225* (1), 203−212.
(97) Schreier, M.; Regalbuto, J. R. A fundamental study of Pt tetraammine impregnation of silica: 1. The electrostatic nature of platinum adsorption. *J. Catal.* **2004**, *225* (1), 190−202.
(98) Uheida, A.; Iglesias, M.; Fontàs, C.; Hidalgo, M.; Salvadó, V.; Zhang, Y.; Muhammed, M. Sorption of palladium(II), rhodium(III), and platinum(IV) on Fe3O4 nanoparticles. *J. Colloid Interface Sci.* **2006**, *301* (2), 402−408.
(99) Badri, A.; Binet, C.; Lavalley, J.-C. Use of methanol as an IR molecular probe to study the surface of polycrystalline ceria. *J. Chem. Soc., Faraday Trans.* **1997**, *93* (6), 1159−1168.
(100) Jaegers, N. R.; Lai, J.-K.; He, Y.; Walter, E.; Dixon, D. A.; Vasiliu, M.; Chen, Y.; Wang, C.; Hu, M. Y.; Mueller, K. T.; et al. Mechanism by which Tungsten Oxide Promotes the Activity of Supported $V_2O_5/TiO_2$ Catalysts for $NO_X$ Abatement: Structural Effects Revealed by $^{51}V$ MAS NMR Spectroscopy. *Angew. Chem., Int. Ed.* **2019**, *58* (36), 12609−12616.
(101) Shubin, A. A.; Lapina, O. B.; Bondareva, V. M. Characterisation of strongly bonded V(V) species in VO/TiO2 catalyst by static and MAS solid-state NMR spectroscopy. *Chem. Phys. Lett.* **1999**, *302* (3−4), 341−346.
(102) Hu, J. Z.; Xu, S.; Li, W.-Z.; Hu, M. Y.; Deng, X.; Dixon, D. A.; Vasiliu, M.; Craciun, R.; Wang, Y.; Bao, X.; et al. Investigation of the Structure and Active Sites of $TiO_2$ Nanorod Supported $VO_x$ Catalysts by High-Field and Fast-Spinning $^{51}V$ MAS NMR. *ACS Catal.* **2015**, *5* (7), 3945−3952.
(103) Wu, Z.; Rondinone, A. J.; Ivanov, I. N.; Overbury, S. H. Structure of Vanadium Oxide Supported on Ceria by Multiwavelength Raman Spectroscopy. *J. Phys. Chem. C* **2011**, *115* (51), 25368−25378.



https://doi.org/10.1021/acs.jpcc.4c02018
J. Phys. Chem. C 2024, 128, 9169−9181